J Mater Sci (2006) 41:5068–5080
DOI 10.1007/s10853-006-0445-5

Experimental evidence of liquid drop break-up in complete wetting experiments

R. Rioboo · M. H. Adão · M. Voué · J. De Coninck

Received: 10 October 2005 / Accepted: 10 March 2006 / Published online: 18 July 2006

Abstract We report experiments concerning the deposition of a droplet on a solid surface and the related spontaneous spreading, during which a secondary droplet is ejected. Experimental investigations and theoretical considerations have been performed in order to understand the reasons of the formation of this droplet and of its ejection and to estimate the conditions that induce these phenomena. High-speed imaging and specific deposition conditions have been necessary to visualize such phenomena. It has been shown that the ejection is possible in the complete wetting regime when low impact inertia and high position of the center of mass of the drop before spreading are achieved simultaneously. A model taking into account non-stationarity, inertia, wetting capillarity and viscous effects has been developed. It resulted in two dimensionless numbers Π_1 and Π_2 that characterize the occurrence of the ejection phenomenon.

Introduction

Drop deposition or impact on solid surfaces is frequently used in industrial processes. It is therefore of interest to control the quality and the outcome of the deposition or of the impact process [1]. On solid flat surfaces, the former has been widely explored in order to understand the dynamics of spontaneous wetting [2–5]. This low inertial process is particularly suitable for exploring wetting phenomena when the impact velocity is kept small [5]. The key experimental parameters that control the spreading are the impact velocity (V), the drop size (D), the liquid physical properties such as the surface tension (σ) and the dynamic viscosity (μ), and the characterization of the solid surface in terms of topography and chemistry [6, 7]. Schiaffino and Sonin [5] showed that the relevant parameters to characterize drop impact and spreading in dimensionless form are the Weber ($We=\rho\ DV^2/\sigma$) and Ohnesorge ($Oh = \mu/\sqrt{\rho D\sigma}$) numbers, where ρ is the liquid density. We, which is the ratio between capillary and impact pressure forces, scales the driving force of the process. Oh, which is the ratio between the intrinsic time for inertial oscillations and the one for their decay by viscous diffusion, scales the resistive effects.

While most experiments are performed with average speed cameras (i.e. 50 or 60 frames per second), only high-speed imaging can provide information about the initial stage of spreading in the case of either spontaneous spreading or of the impact of a droplet on liquid or solid surfaces [8–11].

At the moment of contact between the liquid drop and the solid surface, the wetting is due to the unbalanced Young force [12] and the system can be understood as a dissipative mechanical system [2]. If low viscosity liquids are used, inertia and surface tension phenomena become dominant [5, 13]. In experiments of deposition of liquid drops on a liquid bath, Thorrodsen and Takehara [8] showed that a droplet ejection cascade can occur. Very recently, Roux and Cooper-White investigated the dynamics of water drop

R. Rioboo (✉) · M. H. Adão · M. Voué · J. De Coninck
Centre for Research in Molecular Modeling, Materia Nova/ Université de Mons-Hainaut, Avenue Copernic 1, 7000 Mons, Belgium
e-mail: romain.rioboo@crmm.umh.ac.be

spreading on a glass surface [14]. In particular, they showed that the deposition of a water drop on glass can result in the ejection of a secondary droplet.

In the present study, carried out simultaneously with Roux and Cooper-White's work, we also investigated this phenomenon but we extend and adequately support some of the results presented in [14], by considering the deposition of various liquids on completely wettable substrates. More specifically, we propose to investigate and explain the formation of such droplets and their ejection in terms of a non-stationary wetting process and the shape of the drop for various liquids. In order to generalize and predict possible ejection, dimensional analysis is investigated in terms of *We* and *Oh*. Predictions based on this analysis are not satisfactory enough. A simple geometrical model of the phenomena is presented hereafter to improve the predictability of the ejection of a secondary droplet.

Geometrical model

Before explaining the spreading of the drop on the solid surface, let us briefly consider its behavior during its fall. In particular, one has to keep in mind that the drop is generally oscillating after its detachment from the needle. As the height of fall is very low, in order to keep inertia as small as possible, the drop is still oscillating when it touches the solid surface and its shape is non-spherical. It is therefore possible to characterize it by two diameters D_H and D_V, respectively measured along the horizontal and vertical directions.

To establish the basic equations of our model (Fig. 1A), let us consider a typical image of a drop spreading on the solid surface (Fig. 1B). The drop is, at a first approximation, made of two parts with distinctive time behaviors: a shrinking reservoir and an expanding cone. The former is moving downward by its inertia. Its mechanical energy determines its impact velocity. The expansion of the cone is driven by inertial capillarity at a spreading speed, denoted by V_{spr}. As $V_{spr} \gg V$ in the first stages of the phenomenon, the global motion of the drop is dominated by the spreading of the cone. Figure 1C presents a possible scheme of the velocity field inside the drop. Due to the conservation of the total volume of the drop, the larger the expansion of the cone, the larger the shrinkage of the sphere. It is reasonable to consider that the liquid molecules which form the upper part of the drop do not interact with the solid surface, so that the sphere is not perturbed yet by the presence of the substrate and continues its motion downward by inertia.

Figure 1D represents a schematic time sequence of the falling and spreading drop. Let us define the origin of the time by the moment at which the droplet touches the solid surface and t_{max}, the characteristic moment at which the totality of the liquid of the initial drop would be up taken by the cone (in case of no ejection). At this time, the volume of the shrinking sphere is zero. To estimate t_{max}, let us now consider the time dependence of the spreading radius, as given by the model of Biance et al. [13] which is valid for the ''early'' stages of the spreading of low viscosity liquids:

$$r = \left(\frac{\sigma D}{2\rho}\right)^{1/4} t^{1/2} \tag{1}$$

Using the hydrodynamic Hoffman–Tanner–Voinov law's [15–17], it is possible to relate the dynamic contact angle, θ, and the spreading velocity:

$$\theta \propto C_{HTV} Ca^{1/3} = C_{HTV}\left(\frac{\mu V_{spr}}{\sigma}\right)^{1/3} \tag{2}$$

where C_{HTV} is an empirical constant close to 4.5 [18]. From geometrical arguments (Fig. 1A) and using the small contact angles approximation, it is possible to calculate θ and H the apex of the expanding cone:

$$H = r\tan(\theta) \cong r\theta \tag{3}$$

In this way, we can approximate H, from Eq. 3, by replacing r and θ by their expression from Eqs. 1 and 2 and using $V_{spr}=dr/dt$. This yields:

$$H = C_{HTV}\left(\frac{\mu D}{4\rho}\right)^{1/3} t^{1/3} \tag{4}$$

Let us now calculate the position of the bottom of the shrinking reservoir as a function of time, considering that this droplet is following its path due to inertia. Assuming that at $t=0$ its center of mass is at height H_G from the solid surface, we have:

$$h = H_G - Vt - r_s \tag{5}$$

where r_s is the radius of the reservoir. As previously defined, t_{max} is the intrinsic time which characterizes the time necessary to transfer the initial volume of the liquid contained in the drop (Ω_0) in a spontaneously expanding cone of volume Ω_1. It can be evaluated as follows. By the conservation of volume ($\Omega_1=\Omega_0$), we obtain for $t=t_{max}$ an equation combining the time dependent quantities H,r and the initial drop diameter D.

$$r(t_{max})^2 H(t_{max}) = D^3/2 \tag{6}$$

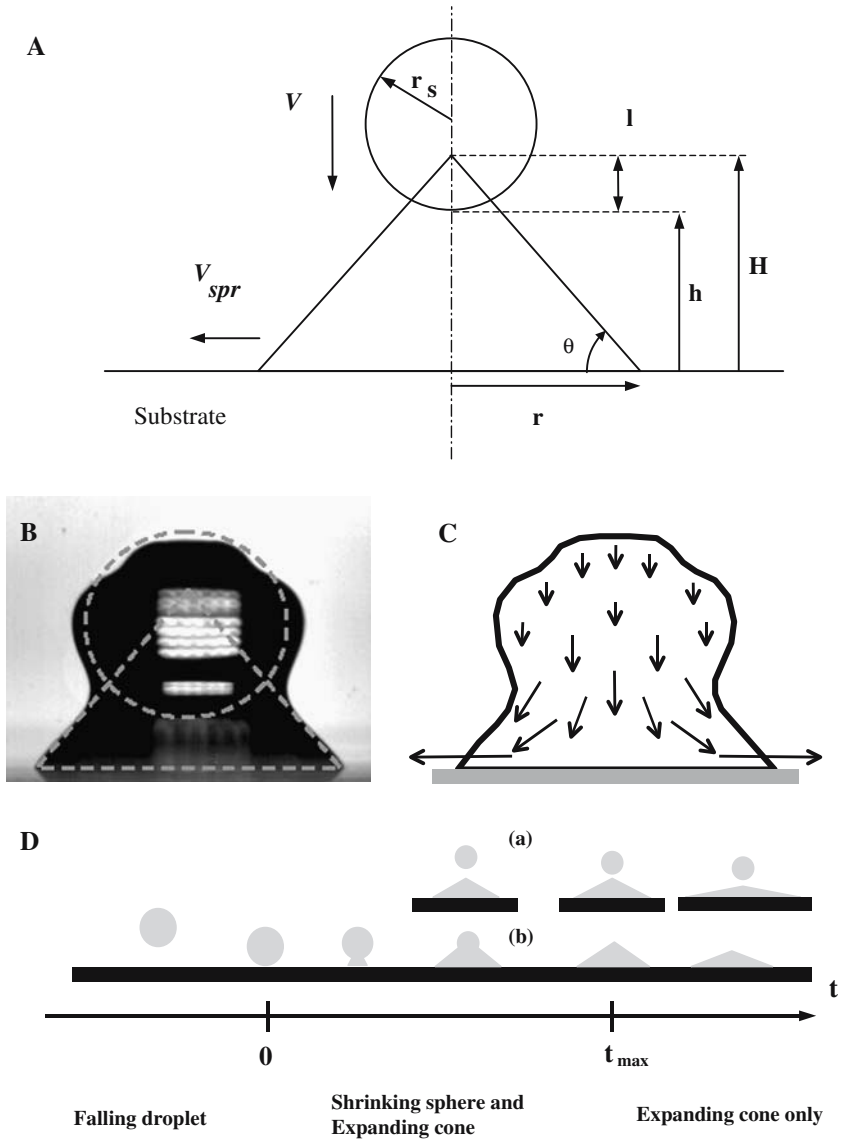

Fig. 1 Drop during its first spreading stages (**a**) Schematic diagram presenting the two parts of the geometrical model (**b**) Example of drop shape (water droplet, diameter: 2.45 mm, impact speed: 0.093 m/s). Dashed lines: basic elements of the model (**c**) Possible scheme of the flow field. In the region of the contact line the velocity is high while in the reservoir region the velocity is uniform and low. (**d**) Time sequence for the falling droplet. Events (a: ''ejection'') and (b: ''no ejection'')

Replacing t by t_{max} in the Eqs. 1 and 4 and substituting their values in Eq. 6 yields a simple expression for the characteristic time

$$t_{max} \approx \left[\frac{D^{13}\rho^5}{\mu^2\sigma^3}\right]^{1/8} \tag{7}$$

If the ejection occurs, it will happen at t $< t_{max}$. For t in the range $0 < t \leq t_{max}$, the occurrence of the 'ejection' event is related to the sign of $l(t)$, the difference between H and h (Fig. 1A). Due to the time dependence of the radius of the shrinking sphere r_s, one obtains a cubic equation in r_s with rather complicated coefficients. It is beyond the scope of the article to discuss this result in detail but the link between $l(t)$ and t_{max} is schematically described in Fig. 1D. More simple is the expression of l_{max}, the value of $l(t)$ at $t=t_{max}$, because r_s vanishes at that time. Combining Eqs. 4, 5 and 7, we explicitly obtain

$$l_{max} = C_{HTV}\left[\frac{\mu^2 D^7}{\rho\sigma}\right]^{1/8} - H_G + V\left[\frac{D^{13}\rho^5}{\mu^2\sigma^3}\right]^{1/8} \tag{8}$$

In a dimensionless form, this equation reads

$$\frac{l_{max}}{H_G} = C_{HTV}\Pi_1 - 1 + \Pi_2 \tag{9}$$

where we have defined two dimensionless numbers Π_1 and Π_2 as

$$\Pi_1 = \left[\frac{\mu^2 D^7}{\rho\sigma H_G^8}\right]^{1/8} = \frac{D}{H_G}Oh^{1/4} \tag{10}$$

$$\Pi_2 = V\left[\frac{\rho^5 D^{13}}{\mu^2\sigma^3 H_G^8}\right]^{1/8} \quad (11)$$

Due to the multiple approximations of this geometrical model, Eq. 9 does not directly help in the prediction of the ejection of the secondary droplet. Nevertheless, it provides a new representation plane Π_1–Π_2 expected to be more efficient than the *We–Oh* representation because it takes into account more specifically the physical characteristics of the addressed problem of deposition of a drop in a complete wetting regime.

As it will be shown hereafter, a confrontation of the results of this simple model with the experimental ones will confirm that Π_1 and Π_2 are better suited to characterize the problem than simply *Oh* and *We*, especially if we use D_V, the diameter of the drop along its vertical axis, instead of D in the Eqs 10 and 11. This can be explained by the lack in modeling the oscillations of the droplet.

Experimental procedure

Chemicals and substrate preparation

Unless otherwise stated, all the chemicals and reagents were analytical grade and purchased from Sigma-Aldrich. They were used as received without further purification. MilliQ water, methanol, ethanol, isopropanol, acetone and a water–glycerol mixture were used for their low viscosity. The physical characteristics of the liquids are reported in Table 1.

The solid surfaces were smooth microscope glass slides (Menzel–Gläser) cleaned in an argon plasma cleaner (Harricks, 30 W at 8 MHz RF) for 5 min. Their root-mean-square roughness, determined by optical profilometry (Wyko NT1100, Veeco Instruments) was 4.6 Å. The chosen liquids completely wet the substrates, within a few tens of second. It is worth noting that the whole ejection event lasts a few tens of milliseconds at maximum, i.e. 10^3 times faster.

Spreading experiments

The liquid drops are formed at the tips of needles of various diameters. Once formed, the droplets detach themselves from the needle and fall by their own weight from different adjustable heights. They exhibit oscillations due to the detachment from the needle and usually have of a non-spherical shape with an aspect ratio, defined by D_V/D_H in the range from 0.6 to 1.095.

The path of the drop before touching the solid surface is so small that a non-negligible amount of oscillation is still present at the moment of solid-liquid contact. The range of physical parameters (drop diameter, impact speed, ...) as well as the dimensionless numbers *We* and *Oh* are presented in Table 2. A C-MOS camera (VossKühler GmbH) was used. Most sequences were performed at 923 images per second with an image resolution of 512×1024 pixels. In a few cases, it was necessary to increase the frame rate to 1846 images per second. A Navitar 6000 objective was used to give a suitable magnification of the image, typically, 14.4 μm/pixel. The impact speed was experimentally varied by changing the height of fall of the drop. To determine this parameter, the height of the center of mass of the drop relative to the solid surface was calculated by mean of image analysis assuming axial symmetry of the drop. This was performed for the image before (H_G) contact between solid and liquid and the one before this one. The difference between these two heights divided by the time step of the camera gives an estimation of the impact velocity, V.

Results and discussion

Figure 2 shows three examples of the spontaneous spreading of a liquid droplet on a dry glass surface. The images sequences (a) and (c) shows the ejection of a secondary droplet while the phenomenon is not observed in the sequence (b). Before the drop makes contact with the solid surface, it is spherical (aspect ratio ≈1; see Fig. 2-a1, b1 and c1). As the liquid approaches the solid surface, a deformation of the

Table 1 Physical properties of the liquids (T = 25 °C): density (ρ), surface tension (σ) and dynamic viscosity (μ)

Liquid	ρ (kg/dm^3)	σ (mN/m)	μ (mPa s)
Water	0.996	72.8	0.89
Methanol	0.791	22.7	0.54
Ethanol	0.789	22.1	1.07
Isopropanol	0.783	20.9	2
Acetone	0.786	23.5	0.3
Glycerol/water mixture (25% v/v)	1.061	70.0	2.17

Table 2 Range of physical parameters of the impact (Min–Max): drop diameter (D), impact speed (V), height of the center of mass at the contact moment (H_G), Weber number (We) and Ohnesorge number (Oh)

Liquid		D (mm)	V (m/s)	H_G (mm)	We	Oh
Water	Min	0.079	0.021	0.04	0.01	0.0016
	Max	5.29	0.403	2.59	3.89	0.0132
Methanol	Min	1.53	0.055	0.47	0.18	0.0029
	Max	2.28	0.096	0.97	0.53	0.0036
Ethanol	Min	1.27	−0.048	0.42	0.02	0.0061
	Max	2.19	0.092	1.12	0.67	0.0080
Isopropanol	Min	1.58	0.043	0.53	0.11	0.0106
	Max	2.27	0.096	0.95	0.74	0.0127
Acetone	Min	0.71	0.036	0.34	0.07	0.0014
	Max	2.71	0.144	1.41	1.29	0.0027
Glycerol/water (25% v/v)	Min	2.55	0.041	0.97	0.07	0.0049
	Max	2.62	0.072	1.27	0.20	0.0050
Global range	Min	0.079	−0.048	0.039	0.011	0.0014
	Max	5.29	0.40	2.59	3.89	0.013

droplet shape appears. Before the effective contact between the liquid and the solid, the aspect ratio can decrease to 0.6 (see Fig. 2-a3). The drop seems to lie on the substrate like a balloon of water, i.e. without spreading. In some sequences, it is possible to see the drop bouncing on the surface while oscillating. At this time apparent contact is only a visual artifact; in fact a film of air exists between the drop and the solid and there is no real contact (Fig. 2 a1–3) [19]. The most logical explanation is that the drop is bouncing on an air cushion that is trapped between the liquid and the solid. While approaching the wall, the drainage of the air between the drop and the solid surface induces a deformation of the free surface and a flattening of the drop [19–21]. This is consistent with the fact that the substrate has a particularly low root-mean-square roughness. When the drop approaches the solid, the liquid at its bottom tends to spread as fast (the systems are complete wetting systems) as the physics of wetting drives it [22], while the liquid in the upper part of the drop tends to remain in the same place due to inertia. The competition between these two contradictory behaviors and the capillary effects leads to the break-up of the drop and more specifically to the ejection of a secondary droplet. This also explains in a simple way the quasi-stationary value of the contact angle, followed by its sudden decrease reported in [14, Fig. 17]. The dynamics of the contact line will be investigated in a forthcoming article.

The study of the drainage of the air cushion is beyond the scope of the present article. Nevertheless, a rough estimation of the time for the drainage [21] yields a time scale of the order of 1 to several milliseconds, i.e. a drainage speed compatible with the acquisition speed of our imaging system. Typically the apparent contact angle decreases from the initial very high values (around 180 degrees) which are difficult to measure, to less than 90 or even 70 degrees, which is easily measurable, in only one frame. We thus assume that the real contact between solid and liquid molecules occurs between those two consecutive images. The time scales presented in Fig. 2 are calculated from the beginning of the spreading based on such an assumption. Thus we assign the time of the first image where spreading is noticed to half of the acquisition time step of the camera. In these particular cases, the first images where spreading is noticeable are shown on images (a3) i.e. $t = 0.5$ ms or (c2) i.e. $t = 0.3$ ms. As experiments are recorded at least at 923 images per second, the maximum time lapse between two consecutive images is 1.083 ms. The error bar on the time is therefore about 0.5 ms.

In fact, because the investigated systems consist of liquids of low viscosity and solids of high surface energy the spontaneous spreading is very fast. The spreading force and the spreading velocity are therefore high (in several cases above 1.5 m/s), particularly at the beginning of the process.

Roux and Cooper-White [14] showed that for low impact velocities on glass, water drops can exhibit ejection of a secondary droplet. They indicated that the impact velocity is the key parameter for the occurrence of this phenomenon. They also mentioned Reynolds ($Re=\rho\ DV_{th}/\mu$) and Weber ($We=\rho\ DV_{th}^2/\sigma$) numbers where they extrapolated the impact velocity V_{th} from the height of fall.

As the droplets imaged in the series (b) and (c) of Fig. 2 have the same impact velocity and almost the same drop diameter (i.e. very similar Re and We values), it becomes evident that neither the sole impact

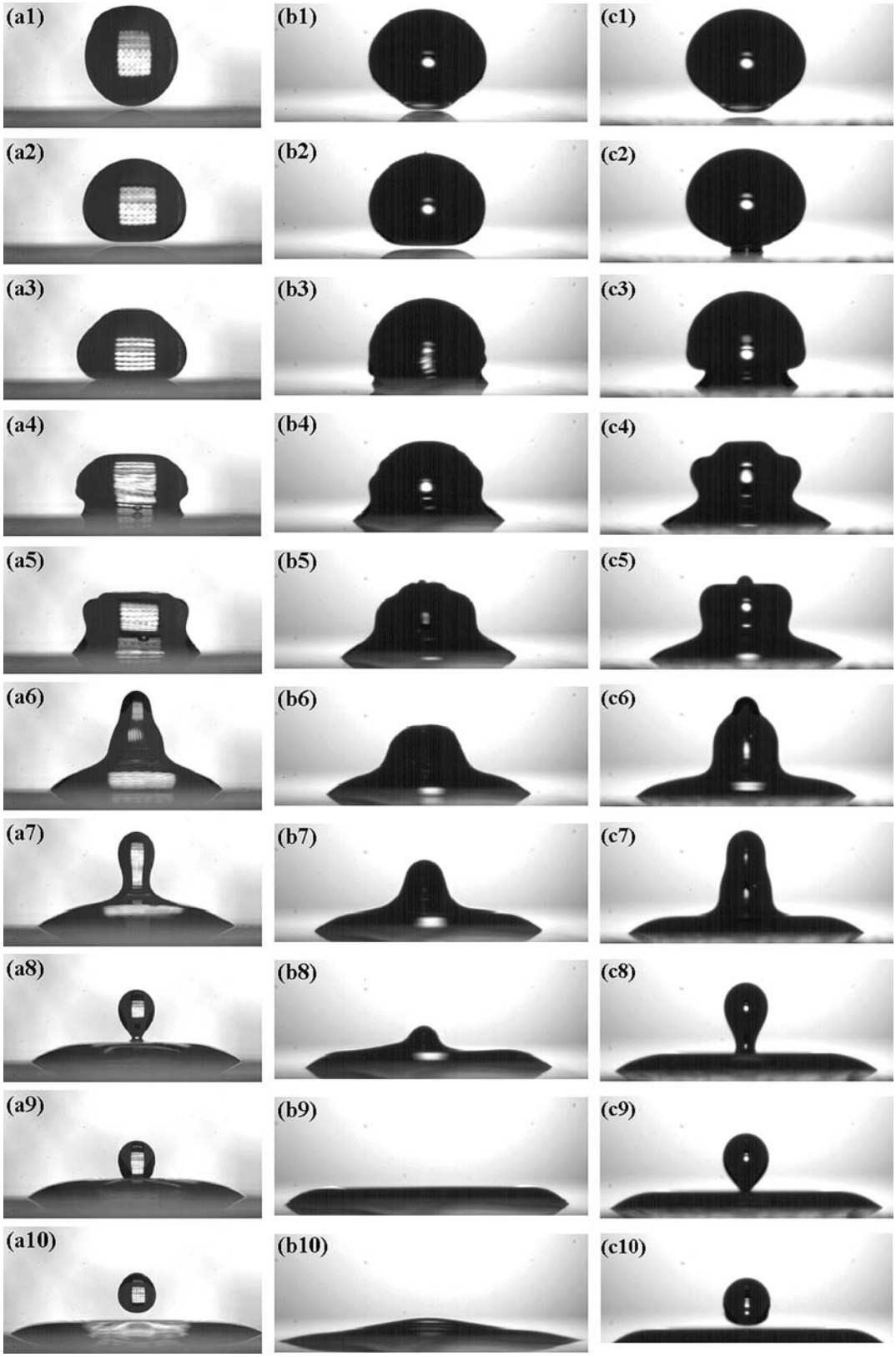

Fig. 2 Deposition process of drops on a clean smooth hydrophilic glass surface with ejection and no-ejection. (**a**) water drop of $D = 3.56$ mm impacting at 0.032 m/s; (**b**) and (**c**) acetone drops of respectively $D = 2.31$ mm and $D = 2.41$ mm both impacting at 0.1 m/s. Times (in ms, for each sequence from 1 to 10) are (*a*): −10.5, −5.5, −1.5, 0.5, 1.5, 4.5, 6.5, 8.5, 9.5, 16.5; (*b*): −2.4, −0.8, 0.8, 1.9, 3, 4.6, 6.2, 7.8, 12.2, 33.3; (*c*): −0.3, 0.3, 1.9, 4.1, 5.1, 6.8, 7.8, 10, 11.1, 11.6

velocity nor *Re* and *We* cannot be the only key parameters to determine whether the ejection will occur or not. Clearly a more general investigation and complementary tests are necessary to determine the condition of ejection.

The drop size is approximated by $D=(D_H^2 D_V)^{1/3}$. A more precise calculation based of the exact shape of the drop (taken from image analysis and supposing an axisymmetric drop) for several cases shows a mean discrepancy of less than 5% with this approximation. The height of the centre of mass, H_G, before spreading has a mean value of approximately 100 pixels, depending on the magnification and on the drop size. This allows an estimation of the relative precision of this parameter to be 1% (Table 2).

We present in Fig. 3 the occurrence of the ''ejection'' and ''no-ejection'' events, for water. The parameters used in this figure are only geometrical and no liquid property is involved. Figure 3 shows that depending on the impact conditions (V, D and H_G), a distinction can be made between both types of events. The same result has been found for each liquid used except isopropanol for which we couldn't find appropriate experimental conditions for ejection. The separating line in terms of H_G versus DV is found to be different (for both the slope and the Y intercept) for each liquid. No warrantee on the uniqueness of this distinction exists on the sole basis of the data analysis. Thus it is necessary to include dimensional and physical analysis in order to generalize these results and be able to predict the ejection in the widest range of experimental conditions.

Our results show break-up of low viscosity liquids drops due primarily to wetting phenomena, but several other physical phenomena are acting: viscous dissipation, surface tension forces, inertia and gravity. It seems clear that when viscous dissipation is too high no break-up is possible, and motion of the liquid in all regions of the drop is too slow.

We suggest that the ejection is due to the opposite motion of the bottom of the drop that tends to spread outwards due to the strong wetting and the top of the drop that tends to ''stay'' in its elevated high position above the solid surface because of its inertia (see Fig. 1A). The spreading velocity is much higher than the velocity of the top of the drop which is moving down at a rate due primarily to inertia. It seems clear that increasing impact velocity will drive the liquid in the quasi-spherical reservoir of the top of the drop further down by inertia. Thus, the higher the impact speed, the less likely we are to observe ejection (see Fig. 3). In other words low momentum of impact of the drop compared to the characteristic speed of wetting is likely to help the break-up.

In the same vein, we recall that at the start of spreading the drop exhibits a non-spherical shape. Thus the higher the position of the centre of mass the more favorable the conditions for droplet ejection.

In Fig. 2, we can notice a capillary wave that is travelling from the contact line upward [14]. The characteristic velocity, V_c, of propagation of this capillary wave is of [22, eq. 5.55 pp122]: $V_c=(2\pi\sigma/\rho\ D)^{1/2}$. Typically, for water drops of 3.5 mm of diameter, this velocity is of the order of 0.36 m/s. Since the speed of

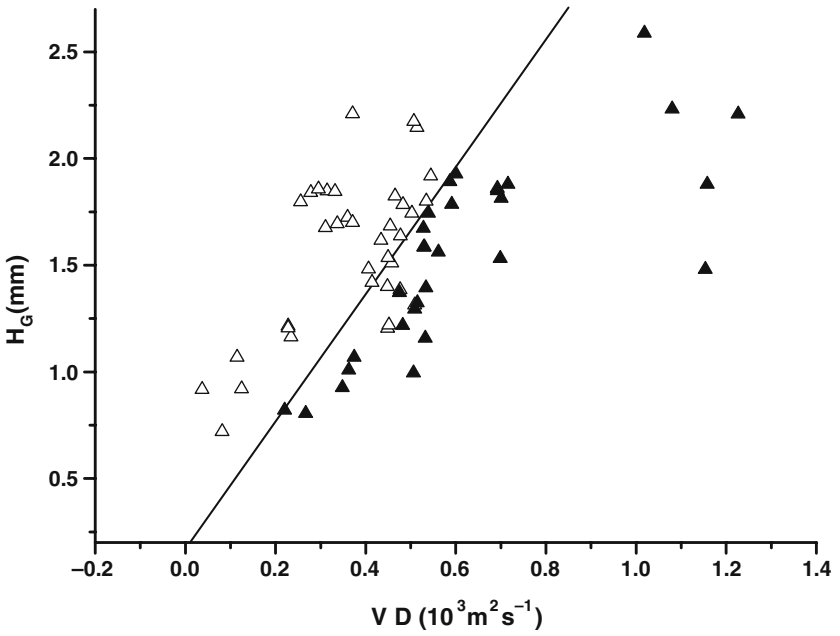

Fig. 3 The height of the centre of mass (H_G) for the water cases studied as a function of the parameter VD. Ejection cases are represented by open symbols and the no ejection cases with full symbols. An empirical limit is presented as a line to guide the eyes

spreading (typically 1 m/s or higher) is faster, the propagating contact line acts as a sink. The unbalanced Young force is pulling the liquid outward radially from the contact line. The liquid in the upper part of the shrinking droplet tends to remain there or to move only slowly with its initial velocity. Since the reservoir isn't receiving the capillary wave while the contact line is still pulling the liquid, a narrow region is necessarily produced (the neck in Fig. 1).

If we consider the experimental data in the *We–Oh* plane [5] we are able in a way to take into account the relative characteristic times (through *Oh*). Figure 4 shows this representation. It is noticeable that increasing both *We* and/or *Oh* lowers the probability to get the ejection. Beyond this trend, it appears that the data clouds represented each type of event are strongly overlapping. The aspect ratio D_V/D_H, has an unambiguous effect (Fig. 2) but cannot directly be taken into account in this representation. One has to use horizontal and vertical diameters to put in evidence the possible effect of this parameter. This can be performed (using D_H and/or D_V instead of D in the dimensionless numbers, for example) and has been tried without real success despite the questionable arguments to justify this.

Let us now try to find a representation of the physical phenomenon, based on the simple geometrical model described in section 2 and let us represent the experimental data in the plane Π_2 versus Π_1(Fig. 5). The improvement of the data separation brought by the new representation is not obvious. Additional criterions are requested to bring evidence that the $\Pi_2-\Pi_1$ plane gives better results than the *We-Oh* plane. Intuitively, the latter takes into account only simple dimensional analysis considerations (Fig. 4) while the aspect ratio of the drop is intrinsically taken into account via H_G and D_V in the $\Pi_2-\Pi_1$ representation of the experimental data. Probably due to the experimental limitations (we have access to the images of the drop every millisecond), the possible errors in analysis and the simplification of the model can explain the overlap between the 'ejection' and the 'non-ejection' zones.

To overcome the drawbacks of the visual comparison between the representations of the data, it seems to us interesting to find a criterion leading to an optimal separation of the two sets of data points (''Ejection'' and ''No Ejection''). This problem is quite similar to optimization problems considered in automatic classification, when it is required to determine the position of an optimal frontier of decision without knowledge of the functional expression of the latter. One of the statistical learning techniques used to solve this kind of problems is the *Support Vector Machines* (SVM) technique, introduced by Vapnik in 1992 [23]. Detailed information about this technique will be found in [24, 25] and in the references therein. It is far beyond the scope of this article to present the mathematical details of the technique. Only a brief overview of the technique is given in Appendix A. In this paragraph, the focus has been made on the results of the classification that validated the new dimensionless parameters Π_1 – Π_2. As seen on Figs. 4 and 5, our data points are not necessarily linearly separable in the input space (here the 2-D spaces of log(*We*)–log(*Oh*) or Π_1 -Π_2). We compared the effect of two different kernels (the linear and the radial ones) on the classification of the events for both types of representation of the data, i.e.

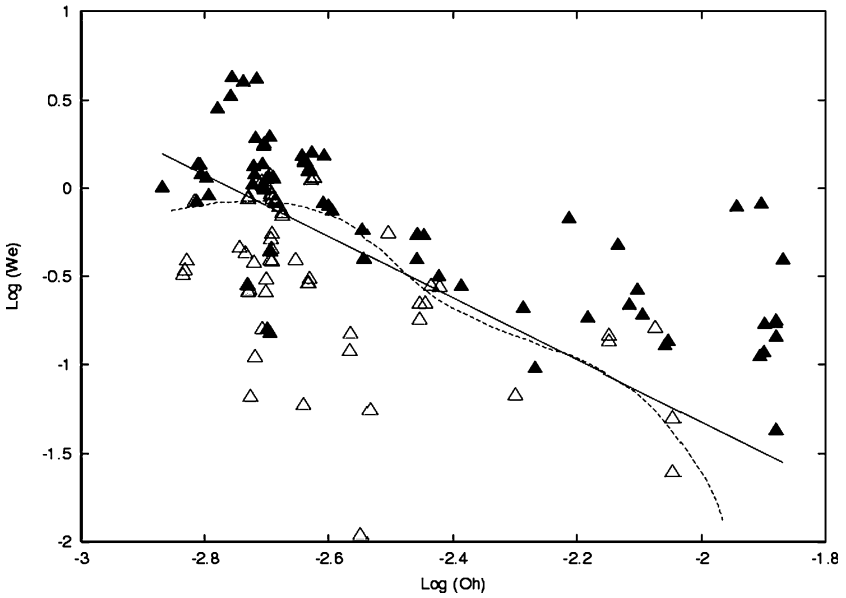

Fig. 4 Ejection (open triangles) and of non-ejection (filled triangles) events in the *We–Oh* plane. The plain and the dashed lines represent the optimum decision frontiers between both types of events, calculated using the linear and the radial kernels respectively. In the linear case, the optimum frontier of decision is given by log(*We*)=–4.812–1.746log (*Oh*)

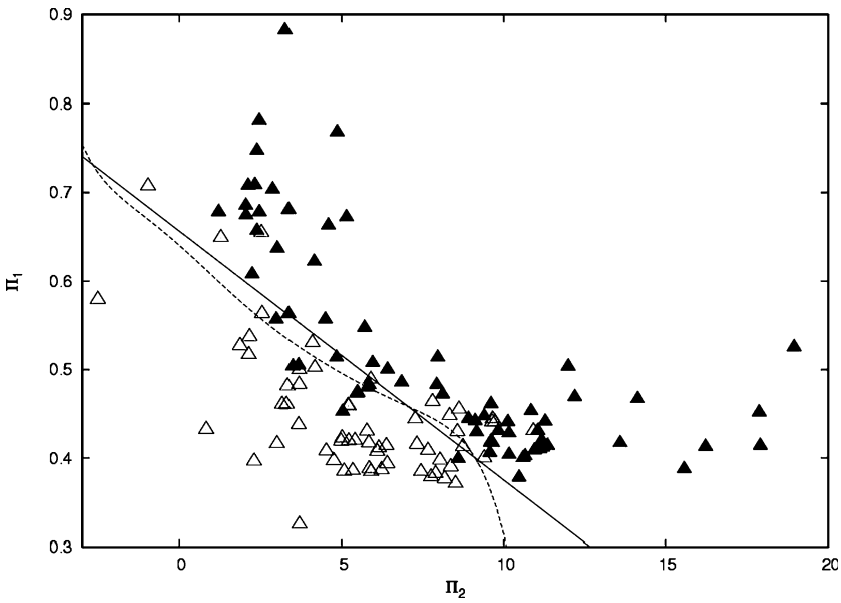

Fig. 5 Same as Fig. 4 but with a representation of the events in the Π_1–Π_2 plane. The optimum frontier is Π_1=0.656–0.028Π_2 (linear kernel). A better separation of the data is obtained in this case (see Table 3)

log(*We*)–log(*Oh*) or Π_1–Π_2. We used the e1071 module [26] of the *R* statistical package [27] to perform the classification. It should be noted that the classification directly depends on the representation of the data: the *We–Oh* and the log(*We*)–log(*Oh*) are therefore not equivalent to each other. The optimum decision frontiers are represented by the plain and the dashed lines in Figs. 4 and 5, for the linear and radial kernels, respectively. Once the frontier has been optimized, the theoretical classification of the events can be compared to the experimental one. The efficiency of the classification can simply be evaluated by the number of incorrectly classified data (Table 3). This number is directly obtained from the sum of the off-diagonal elements of the contingency table between the experimental and theoretical classification data.

The classification of the 132 experimental data appears to be more efficient in the Π_1 -Π_2 plane than in the log(*We*)–log(*Oh*) plane, whatever the type of kernel: the number of incorrectly classified data is less in the former case than in the latter. Changing the type of the kernel function from linear to radial only improves the classification in the log(*We*)–log(*Oh*) plane. For the linear kernel, an explicit equation of the optimum separation line can be obtained. In the Π_1–Π_2 representation of the data, the optimum frontier is Π_1=0.656–0.028Π_2 whereas in the log(*We*)–log(*Oh*) plane, the optimum frontier of decision is given by log(*We*)=–4.812–1.746 log(*Oh*). It should be noted that in the case of the radial kernel, determining an explicit equation for the optimal decision frontier is not possible anymore because the transformation from the input space to the features space is implicit and defined only through the kernel (cfr Appendix A).

Table 3 Number of incorrectly classified data. The classification of the 132 experimental data in the Π_1–Π_2 plane gives better results than in the log (*We*)–log (*Oh*) plane

Kernel	Representation of the experimental data (n = 132)	
	Π_1–Π_2	log(*We*)–log (*Oh*)
Radial	23 (17.4%)	31 (23.5%)
Linear	23 (17.4%)	33 (25.0%)

Changing the type of the kernel function from linear to radial only improves the classification in the log(*We*) –log(*Oh*) plane

Conclusion

The phenomenon of satellite droplet ejection during the deposition and spontaneous spreading of a drop has been studied and measured experimentally in a systematic way. Because of the high unsteadiness of the phenomenon and its rapidity, high-speed imaging was necessary. Several liquids were tested and showed the generality of the phenomenon for complete wetting systems and the right deposition conditions. These conditions under which the ejection occurs were also investigated in detail. High wetting, low viscous dissipation, low impacting inertia and high position of the centre of mass of the drop at the moment of contact were necessary to induce the break-up phenomena. A simplified model was developed and helped in understanding the phenomena. From the model, two characteristic dimensionless numbers Π_1 and Π_2 were calculated. The representation of the experimental data in the Π_2 versus Π_1 could relatively successfully separate the events ‘‘ejection’’ and ‘‘non-ejection’’.

The validity of this representation is supported by the results of SVMs calculations which minimize the number of incorrectly classified data in the Π_1–Π_2 representation. From this work, the results of Thorrodsen and Takehara [8] on liquid–liquid systems can be understood in terms of high speed wetting phenomena.

Acknowledgments This study has been partially supported by the Région Wallonne in the program FEDER Objective I and the European Community. We would like to thank Dr I.V. Roisman and Dr G. Lemaur for fruitful discussions.

Appendix A

The aim of this appendix is to briefly present the Support Vector Machine (SVM) automatic classification technique. It is based on the references [23–25]. Implementations of the technique in the statistical software *R* [27] is derived from the work of Chang and coworkers [26].

Definition of the classification task

The classification task can be defined as finding a rule which, based on experimental observations, assigns an event to one of the predefined classes. In the problem we considered in this paper, the number of classes is 2 (''Ejection'' and ''No ejection'').

Solving the problem is equivalent to finding a function $f{:}R^N \rightarrow \{-1,+1\}$ using a set of training data

$$(\mathbf{x}_1, y_1), \cdots, (\mathbf{x}_n, y_n) \in R^N \times Y, Y = \{-1; +1\} \qquad \text{(A1)}$$

that will correctly classify unseen data (x,y), where **x** is a vector containing the experimental observations. In our case, **x** is defined in R^2. The vectors are denoted by boldface symbols.

Margin and linear classifiers

Let us assume that the experimental data are separable by a hyperplane (in our case, by a straight line). This means that we choose classifiers whose equation is given by

$$f(\mathbf{x}) = \langle \mathbf{w}, \mathbf{x} \rangle + \mathbf{b} \qquad \text{(A2)}$$

where $\langle\ ,\ \rangle$ denotes the inner product in R^N. A linear classifier is therefore defined by a vector **w** normal to the hyperplane and by an offset b. As shown in Fig. A1, it is obvious that for a set of separable data, several valid hyperplanes can be used as classifiers but only one can be considered as the optimum one.

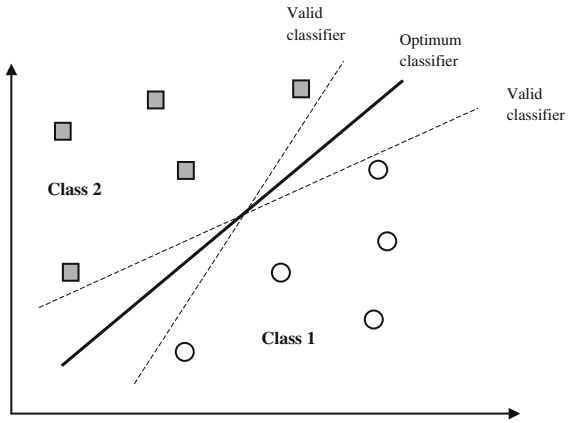

Fig. A1 Schematic representation of the classification problem—Valid (dashed lines) versus optimum (plain lines) linear classifiers

This optimum separation plane can be defined by maximizing the margin. This quantity is defined as the minimum distance of any data point to the classifier (hyperplane in the linear case). The margin can be measured by the length of **w** as follows (Fig. A2a). As a working hypothesis, we have assumed that the observations were (linearly) separable. **w** and b can be rescaled such that the points closest to the hyperplane satisfy $|\langle \mathbf{w}, \mathbf{x}_i \rangle + b| = 1$. If we consider two observations $\mathbf{x}_1$ and $\mathbf{x}_2$ from different classes (''Ejection'' or ''No-ejection'' in our wetting problem), i.e.

$$\langle \mathbf{w}, \mathbf{x}_1 \rangle + b = 1 \text{ and } \langle \mathbf{w}, \mathbf{x}_2 \rangle + b = -1 \qquad \text{(A3)}$$

the margin is given by the distance between these two points, measured perpendicular to the hyperplane, i.e. $2/\|\mathbf{w}\|$, where $\|\mathbf{w}\|$ is the norm of **w**.

Non-linear classifiers

In some cases, a linear classifier is not suitable to perform the classification of the data, even for separable data sets. A non-linear mapping Φ of the data is used and the transformation Φ has to be chosen in such a way that the transformed data are linearly separable in the destination space, named the ''feature space'' *F* (Fig. A3). $\Phi{:}R^N \rightarrow F$ maps the data **x** on $\Phi(\mathbf{x})$. The dimension of *F* is usually higher than N. After the transformation of the data, one works with

$$(\Phi(\mathbf{x}_1), y_1), \cdots, (\Phi(\mathbf{x}_n), y_n) \in F \times Y, Y = \{-1; +1\} \qquad \text{(A4)}$$

It should be noted that the classification is not related to the dimensionality but to the complexity of the classifier. A classical example of non-linear transformation is the following:

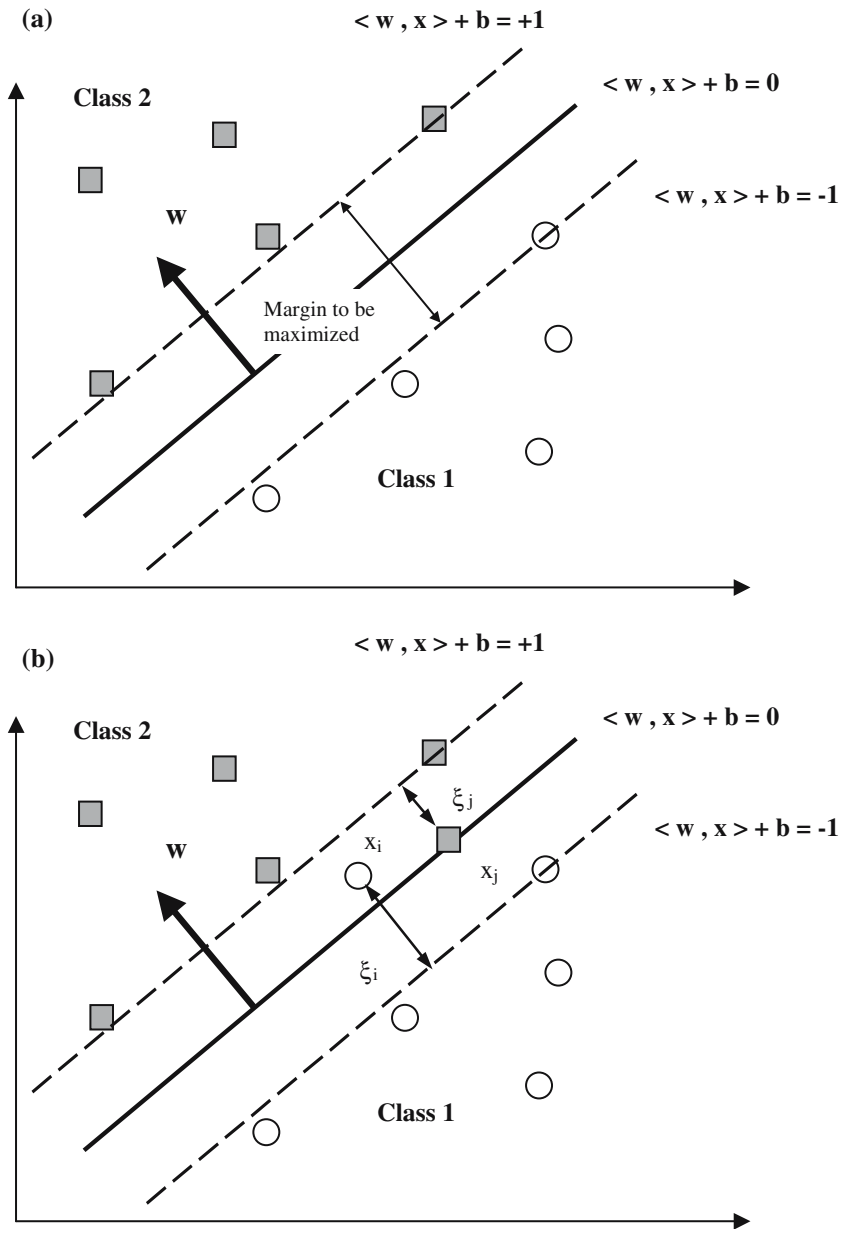

Fig. A2 Schematic representation of the optimum boundary between classes 'I' and 'II' in (**a**) the linearly separable case and (**b**) the non separable case (ξ_i is the penalty given to the incorrectly classified data point)

$$\Phi : R^2 \rightarrow R^3$$
$$(x_1, x_2) \rightarrow (z_1, z_2, z_3) = (x_1^2, \sqrt{2}x_1x_2, x_2^2) \tag{A5}$$

But the advantage of this non-linear transformation stays in the fact that it has not to be explicitly defined. One can easily show that $\langle \Phi(\mathbf{x}), \Phi(\mathbf{x'}) \rangle = \langle \mathbf{x}, \mathbf{x'} \rangle^2$. This means that the inner product in the feature space can be reformulated in terms of a kernel function $k(\mathbf{x},\mathbf{x'})$, without the explicit definition of $\Phi(\mathbf{x})$. In the last example, $k(\mathbf{x},\mathbf{x'}) = \langle \mathbf{x}, \mathbf{x'} \rangle^2$. Besides the simplest (i.e. linear) kernel which is applied to linearly separable data sets, one of the most frequently used kernel is the *radial basis function* (RBF or radial) kernel defined by $k(x, y) = \exp(-\gamma \|x - y\|^2)$, where γ is a positive constant. Several other kernel functions exist (polynomial, sigmoïdal, inverse multiquadratic). Their existence condition is given by Mercer's theorem [28].

Optimization and quadratic programming

Let us first recall that maximizing the margin is equivalent to minimizing $\|\mathbf{w}\|^2$ under constraints. The conditions for perfect classification are (linear classifier)

$$y_i(\langle \mathbf{w}, \mathbf{x}_i \rangle + b) \geq 1, i = 1, \ldots, n \tag{A6}$$

or for the non-linear classifiers,

$$y_i(\langle \mathbf{w}, \Phi(\mathbf{x}_i) \rangle + b) \geq 1, i = 1, \ldots, n \tag{A7}$$

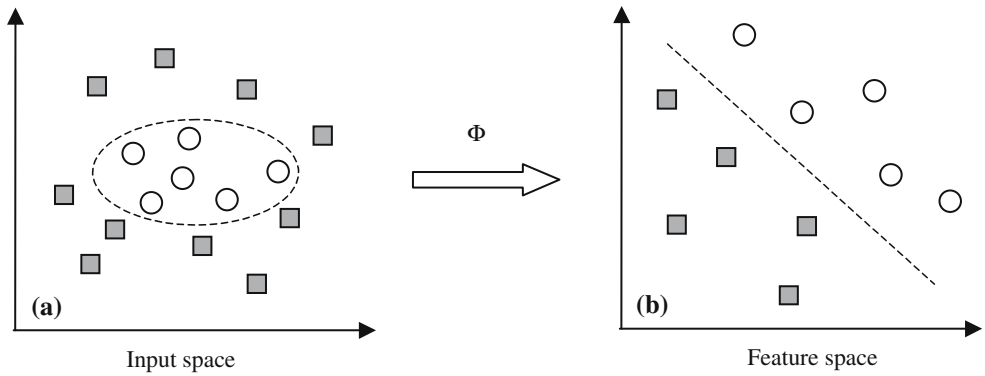

Fig. A3 Schematic representation of the classification problem (**a**) in the input space and (**b**) in the feature space after a non-linear transformation Φ of the data

As the access to the feature space is only possible via the inner products computed by the kernel function, the direct minimization of $\|\mathbf{w}\|^2$with respect to **w** and b is not possible. Nevertheless, one can get rid of this drawback by transforming the primal optimization problem in the dual one. Introducing the Lagrange multipliers α_i (i = 1,...,n) for the constraints (A7), one gets the Lagrangian:

$$L(\mathbf{w},b,\alpha)=\frac{1}{2}\|\mathbf{w}\|^2-\sum_{i=1,n}\alpha_i[y_i(\langle\mathbf{w},\Phi(\mathbf{x}_i)\rangle+b)-1] \tag{A8}$$

As explained in [25], the optimization task is to minimize (A8) with respect to **w**, b and to maximize it with respect to α_i. Equating the partial derivatives of $L(\boldsymbol{w},b,\alpha)$ with respect to b and **w** to zero yields

$$\sum_{i=1,n}\alpha_i y_i=0 \tag{A9a}$$

$$\mathbf{w}=\sum_{i=1,n}\alpha_i y_i\Phi(\mathbf{x}_i) \tag{A9b}$$

Replacing (A9b) in (A8) and substituting $\langle\Phi(\mathbf{x_i}),\Phi(\mathbf{x_j})\rangle$ by its kernel expression $k(x_i,x_j)$, one gets the dual formulation of the optimization problem:

$$\max_{\alpha}\sum_{i=1,n}\alpha_i-\frac{1}{2}\sum_{i,j=1,n}\alpha_i\alpha_j y_i y_j k(x_i,x_j) \tag{A10a}$$

subject to

$$\begin{aligned}&\alpha_i\geq 0, i=1,\ldots,n\\&\sum_{i=1,n}\alpha_i y_i=0\end{aligned} \tag{A10b}$$

Many of the optimized values of α_i are zero and the x_i corresponding to the m non-zero α_i are called support vectors (SV). After the optimization step, the decision function can be calculated as

$$f(\mathbf{x})=\operatorname{sgn}\left(\sum_m y_i\alpha_i k(\mathbf{x},\mathbf{x}_i)+b\right) \tag{A11}$$

where the subscript m runs over all the support vectors. Eq. A11 can be used to visualize the results of the classification: for each of the $\mathbf{x}_j$ (j = 1,... n), one calculates the output $f(\mathbf{x_j})$ and compares it with the observed value y_j. The number of incorrectly classified data corresponds to the number of data for which the product $y_j f(\boldsymbol{x}_j) = -1$ and can be obtained from the contingency table of the variables y_j and $f(\boldsymbol{x}_j)$.

More complicated is the classification of non separable data sets. Typically due to the experimental errors or to some limitations of the models used to transform the data to be classified, an overlap between the data clouds can occur. This is precisely the case in our ejection problem. This means that the conditions for perfect classification (Eqs. A6 or A7) will not be satisfied for all the ($\mathbf{x}_i$,y_i), i = 1, ...,n (Fig. A2b). If the condition (A6) cannot be satisfied, the corresponding α_i will tend to infinity. To get rid of this, one introduces the '*soft-margin*' concept. The constraint is modified to

$$y_i(\langle\mathbf{w},\mathbf{x}_i\rangle+b)\geq 1-\xi_i, i=1,\ldots,n \tag{A12}$$

with $\xi_i\geq 0$ and a penalty $\sum_{i=1,n}\xi_i$ is added to the objective function to be minimized. The primal optimization problem for non separable data is a modified version of (A8):

$$\min\left[\frac{1}{2}\|\mathbf{w}\|^2+C\sum_{i=1,n}\xi_i\right] \tag{A13}$$

where C is the regularization constant which determines the trade-off between the empirical error and the complexity term. The corresponding dual problem is

$$\max_{\alpha} \sum_{i=1,n} \alpha_i - \frac{1}{2} \sum_{i,j=1,n} \alpha_i \alpha_j y_i y_j k(x_i, x_j) \tag{A14a}$$

subject to

$$0 \le \alpha_i \le C, i = 1, \ldots, n$$
$$\sum_{i=1,n} \alpha_i y_i = 0 \tag{A14b}$$

The comparison between (A14) and (A10) shows that only the constraints on the Lagrange multipliers have been modified: they now have an upper and a lower limit.

References

1. Rioboo R, Marengo M, Tropea C (2001) Atomization Sprays 11:155
2. de Ruijter MJ, De Coninck J, Oshanin G (1999) Langmuir 15:2209
3. de Ruijter MJ, Charlot M, Voué M, De Coninck J (2000) Langmuir 16:2363
4. Cazabat AM, Gerdes S, Valignat M-P, Villette S (1997) Interface Sci 5:129
5. Schiaffino S, Sonin AA (1997) Phys Fluids 9:3172
6. de Gennes PG (1985) Rev Mod Phys 57:827
7. Voué M, Rioboo R, Bauthier C, Conti J, Charlot M, De Coninck J (2003) J Euro Ceram Soc 23:2769
8. Thoroddsen ST, Takehara K (2000) Phys Fluids 12:1265
9. Rioboo R, Marengo M, Tropea C (2002) Exp Fluids 33:112
10. Rioboo R (February, 2001) Impact de gouttes sur surfaces solides et sèches. PhD Thesis, University Pierre et Marie Curie, Paris 6, France
11. Rioboo R, Bauthier C, Conti J, Voué M, De Coninck J (2003) Exp Fluids 35:648
12. Brochard-Wyart F, de Gennes PG (1992) Adv Colloid Interface Sci 39:1
13. Biance A-L, Clanet C, Quéré D (2004) Phys Rev E 69:16301
14. Roux DCD, Cooper-White JJ (2004) J Colloid Interface Sci 277:424
15. Hoffman RL (1975) J Colloid Interface Sci 50:228
16. Tanner LH (1979) J Phys D 12:1473
17. Voinov OV (1976) Fluid Dyn 11:714
18. Kistler SF (1993) In: Berg JC (ed) Wettability, Marcel Dekker Inc., New-York
19. Karl A, Anders K, Rieber M, Frohn A (1996) Part Part Syst Charact 13:186
20. Goodall DG, Gee ML, Stevens GW, Beaglehole D (1999) Langmuir 15:4579
21. Bazhlekov IB, Chesters AK, van de Vosse FN (2000) Int J Multiphase Flow 26:445
22. de Gennes PG, Brochard-Wyart F, Quéré D (2002) Gouttes, bulles, perles et ondes, Belin, Paris
23. Boser B, Guyon I, Vapnik V (1992) In: Proceedings of the Fifth Annual Workshop on Computational Learning Theory
24. Vapnik V (1995) The nature of statistical learning theory. Springer-Verlag, New York
25. Müller KR, Mika S, Rätsch G, Tsuda K, Schölkopf B (2001) IEEE Trans Neural Netw 12:181
26. Chang CC, Lin CJ (2001) LIBSVM: a library for support vector machines Software available at http://www.csie.ntu.edu.tw/~cjlin/libsvm.
27. R Development Core Team (2004) R: A language and environment for statistical computing. R Foundation for Statistical Computing, Vienna, Austria. Software available at http://www.R-project.org.
28. Mercer J (1909) Philos Trans Roy Soc London A 209:415